# Dual-Band, Differentially-Fed Filtenna with Wide Bandwidth, High Selectivity and Low Cross-Polarization

Dajiang Li, Ming-Chun Tang, Yang Wang, Kun-Zhi Hu, and Richard W. Ziolkowski

***Abstract* — A compact dual-band, differentially-fed filtenna with wide bandwidth, high selectivity and low cross-polarization is presented. It is composed of a slot-loaded rectangular patch, two pairs of shorting pins, a pair of novel differential coupling feedlines and a defected ground structure (DGS). Good broadside radiation patterns with an adjustable frequency ratio (FR) between its two bands are realized. A pair of U-shaped slots is loaded on the patch to enhance the bandwidth of the lower passband. The DGS and its compact differential feedlines produce five out-of-band radiation nulls to improve the frequency selectivity of the two passbands. Simultaneously, extra in-band resonances are introduced that broaden the impedance bandwidth while maintaining a compact, 0.155 $\lambda_0^2$ aperture size and a relatively low profile (0.065 $\lambda_0$ height). Prototypes were fabricated, assembled, and tested. The measured results, in agreement with their simulated values, demonstrate that it exhibits –10-dB fractional impedance bandwidths of 17.5% and 8.2%, peak realized gain values of 8.4 and 9.5 dBi, and cross-polarization levels smaller than –44 and –40 dB, in its lower and upper passbands, respectively. Its dual-band quasi-elliptic responses have sharp roll-off rates and high stopband suppression levels.**

***Index Terms* — Differential-fed antennas, dual-band antennas, filtennas, high selectivity, low cross-polarization, wide bandwidth.**

## I. Introduction

With future wireless communication technologies dynamically evolving, there is an enormous demand for compact multi-frequency and multi-function antenna systems. Each of these systems involves an ever increasing number of highly integrated components. Filtennas are one of the recently popular multi-functional integrated systems. They combine bandpass filters and antennas into a single device to perform both the filtering and radiating functions simultaneously. Various filtennas have been reported in recent years including single-band [1]-[5], dual-band [6]-[10], and multi-band filtennas [11].

Differential-fed antennas [12]-[20] have also gained considerable attention because of their advantages of easy integration with widely applied differential circuits and systems in comparison to single-feed ones. They require no additional conversion devices, e.g., 180° baluns or hybrid couplers. Hence, they facilitate less complex structures, lower losses, and even lower costs. Moreover, they have many favorable characteristics including harmonic suppression; symmetric radiation patterns; and low cross-polarization levels [17]. Typical examples that have been reported include differential microstrip filtennas [12], [13]; differential dielectric resonator filtennas [14], [15]; differential dielectric patch filtennas [16]; and differential quasi-Yagi filtennas [17]. However, these examples are restricted to single-band operation. They cannot meet the requirements of multi-band systems that are currently common in practical operating environments.

On the other hand, there have been some dual-band differential-fed filtennas (DBDFs) reported [18]-[20]. In particular, an H-shaped slot was etched on a patch antenna in [18] to obtain dual-band operation along with one radiation null. Two open-stub coupling feedlines were introduced to offer two extra radiation nulls to improve the roll-off rates at the band-edges. Nevertheless, the bandwidths of its two bands were only 1.3% and 0.7% due to only a single resonant mode being present in each band. A filtenna with two pairs of differential ports tailored for diplexer applications [19] was realized by replacing the last stage of a second-order Chebyshev filter network with a dual-mode radiator. The bandwidths of its two bands were only 2.4% and 5.2% since only two resonant modes were present in each band. Additionally, there were no radiation nulls produced in either band. Dual operating bands, as well as a natural radiation null between them, were achieved in [20] by etching a pair of slots on each side of a square patch and by introducing a novel feeding structure with open-ended stepped-impedance resonators. The latter were adopted to generate two extra in-band resonances to enhance the bandwidth. Moreover, two extra nulls were introduced to improve selectivity. However, the system occupied a large transverse size and had a relatively high profile.

In this Communication, we develop a novel compact, wideband DBDF with high selectivity and low cross-polarization. It consists of one patch loaded with slots and shorting pins over a defected ground structure (DGS) and a pair of novel differential feedlines. This arrangement is compact and low profile. It facilitates the excitation of the $TM_{01}$ and sidelobe-suppressed $TM_{03}$ modes of the patch to attain the dual-band operation. Extra in-band resonances are introduced to broaden the bandwidth. The slot shapes and the shorting pins enhance the bandwidth of the lower passband and control the frequency ratio (FR) between the two bands, respectively. The DGS and the feed structures produce five independently controllable stopband radiation nulls to improve the roll-off skirts of the two passbands.

## II. The Configuration and Working Mechanism of the Developed DBDF

### *A. Filtenna Configuration*

Fig. 1 depicts the developed DBDF's configuration. As shown in Fig. 1(a), its major features are a slots-loaded radiating patch, two pairs of shorting pins, a pair of novel compact differential coupling feedlines, and a DGS. The filtenna is fabricated with two Rogers RO4003 substrates with relative permittivity $\varepsilon_r$ = 3.55, dielectric loss tangent $tan\ \delta$ = 0.0027. An air gap of height $H_1$ is introduced between

Manuscript received on July 22, 2021; revised on October 24, 2021, revised on November 12, 2021, and revised on December 08, 2021.

This work was supported in part by the National Natural Science Foundation of China contract number 61922018; in part by the Chongqing Natural Science Foundation contract number cstc2019jcyjjqX0004; and in part by the Australian Research Council grant number DP160102219.

D. Li, M.-C. Tang, and Y. Wang are with the Key Laboratory of Dependable Service Computing in Cyber Physical Society Ministry of Education, School of Microelectronics and Communication Engineering, Chongqing University, Chongqing 400044, China (E-mail: tangmingchun@cqu.edu.cn).

K. -Z. Hu is with the Key Laboratory of Industrial Internet of Things and Networked Control, College of Automation, Chongqing University of Posts and Telecommunications, Chongqing, 400065, China.

R. W. Ziolkowski is with the University of Technology Sydney, Global Big Data Technologies Centre, Ultimo NSW 2007, Australia (E-mail: richard.ziolkowski@uts.edu.au).

the two substrates to achieve a good impedance matching. Port 1 and Port 2 are fed by 50-Ω connectors with an inner conductor radius *R*. The two ports are excited with equal amplitude but opposite phase.

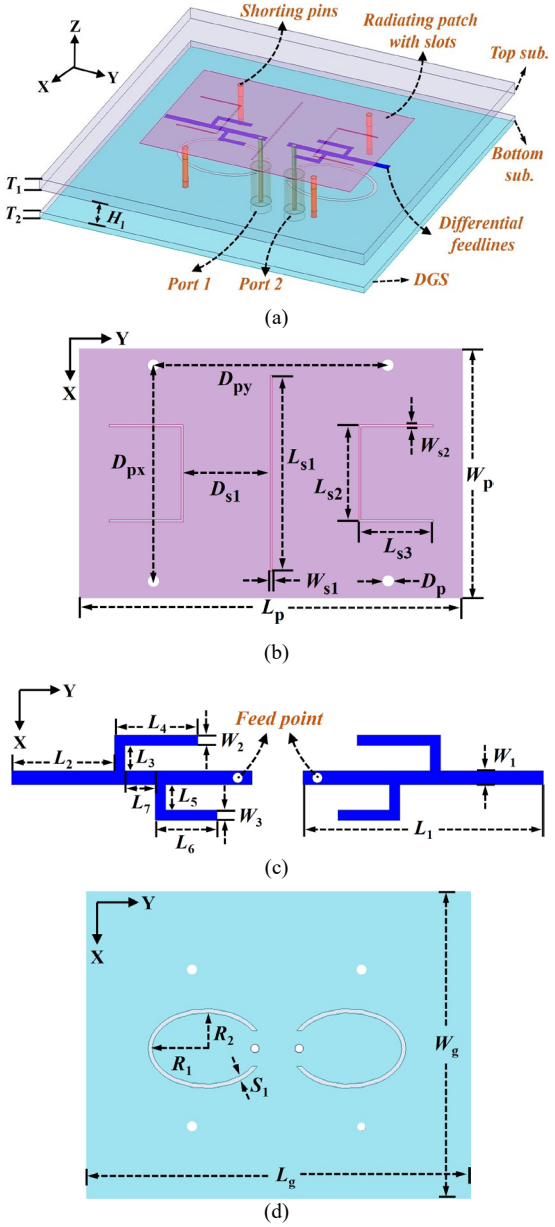


Fig. 1. DBDF configuration and its design parameters. (a) 3-D isometric view. (b) Upper surface of the top substrate. (c) Lower surface of the top substrate. (d) Lower surface of the bottom substrate.

As depicted in Fig. 1(b), the radiating patch is located on the upper surface of the top substrate. Its arrangement yields the $TM_{01}$ and $TM_{03}$ modes of the patch for the dual-band operation. A narrow rectangular slot is etched on it to help reshape the radiation pattern of its $TM_{03}$ mode. Furthermore, the shorting pins and a pair of U-slots load the patch to control the FR between the two working bands and to enhance the bandwidth of the lower passband, respectively. As Figs. 1(c) and 1(d) illustrate, a pair of compact differential coupling feedlines with multiple open-ended stubs are printed on the lower surface of the top substrate. The DGS is located on the lower surface of the bottom substrate. It is composed of a pair of open olive-shaped rings.

This configuration yields five radiation nulls which improve the selectivity of the two operating bands at their band-edges. Concurrently, extra in-band resonances are introduced. They broaden the impedance bandwidth while leaving the physical size and relatively low profile of the antenna the same. The working mechanisms of this filtenna are presented in detail in Section B. The detailed dimensions of the developed DBDF are tabulated in Table I.

TABLE I. OPTIMIZED DESIGN PARAMETERS OF THE DEVELOPED DBDF (DIMENSIONS IN MILLIMETERS)

| | | | | |
|---|---|---|---|---|
| $L_1 = 18.7$ | $L_2 = 8.0$ | $L_3 = 2.0$ | $L_4 = 6.5$ | $L_5 = 2.0$ |
| $L_6 = 4.8$ | $L_7 = 2.5$ | $L_p = 39.0$ | $W_p = 25.6$ | $L_g = 80.0$ |
| $W_g = 80.0$ | $D_{s1} = 8.8$ | $D_{px} = 22.0$ | $D_{py} = 23.8$ | $D_p = 1.0$ |
| $L_{s1} = 20.0$ | $L_{s2} = 9.9$ | $L_{s3} = 7.5$ | $W_{s1} = 0.2$ | $W_{s2} = 0.2$ |
| $W_1 = 1.1$ | $W_2 = 0.8$ | $W_3 = 0.8$ | $T_1 = 1.513$ | $R = 0.45$ |
| $T_2 = 0.813$ | $H_1 = 3.2$ | $R_1 = 7.5$ | $R_2 = 5.0$ | $S_1 = 0.6$ |

### *B. Working Mechanisms*

To analyze the working mechanisms of the DBDF, two steps are emphasized. The first one is the construction of its two operating bands. The second one is to further expand the impedance bandwidth of each one and simultaneously to improve their frequency selectivity and, hence, to enhance their out-of-band suppression levels.

*Step 1) Determining the two operating bands*

The ability to construct the two operating bands is demonstrated nicely by comparing three different sequential versions of a planar microstrip patch antenna (MPA) design. All three are differentially excited by two direct-probe-feeds realized with 50-Ω coaxial connectors. Each one is a two layer design with an air gap whose height is 3.2 mm between the patch and the ground plane. They are illustrated in Fig. 2 for ease of comparison and description.

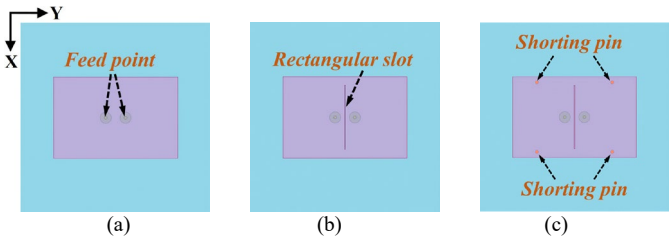


Fig. 2. Three different planar differentially-fed MPA designs. (a) Conventional MPA. Same MPA modified with (b) one rectangular slot and (c) one rectangular slot and two pairs of shorting pins.

It is well known that if a differential feed is used in a conventional MPA, the design can only excite the odd-order resonant modes: $TM_{01}$, $TM_{21}$, $TM_{03}$…, of the patch, i.e., the even-order resonant modes: $TM_{02}$, $TM_{12}$…, are fully rejected [21]. According to the cavity-mode analysis of a patch antenna [22], the resonance frequencies, $f_{mn}$, of the $TM_{mn}$ modes of the differentially-fed MPA in Fig. 2(a) are determined as:

$$f_{mn} = \frac{c}{2\sqrt{\varepsilon_{eff}}}\sqrt{\left(\frac{m}{W_P}\right)^2 + \left(\frac{n}{L_P}\right)^2} \quad (1)$$

where $c$ represents the speed of light and $\varepsilon_{eff}$ is the effective dielectric constant of the substrate. The nonnegative integers $m$ and $n$ are the mode indices along the $x$- and $y$-axis directions, respectively. The parameters $W_P$ and $L_P$ stand for the patch width along the $x$-axis and the patch length along the $y$-axis directions, respectively.

With these choices, the $TM_{21}$ mode occurs out of the frequency range between the $TM_{01}$ and $TM_{03}$ modes when $W_p$ is less than 0.707 times $L_P$. Thus, there are no modes that can be excited between the frequencies of the $TM_{01}$ and $TM_{03}$ modes. Since these modes have the same polarization and broadside properties, there are no modes that could impact those radiation performance characteristics. On the other hand, the sidelobe levels in the *E*-plane (*y*-direction) of the radiation pattern of the $TM_{03}$ mode are significantly high. This sidelobe property must be avoided if truly unidirectional radiated fields are desired.

Referring to [23] for a solution, a non-resonant narrow rectangular slot is loaded along the center of the patch in the *x*-direction, as shown in Fig. 2(b). It reduces the sidelobe levels. Moreover, while the peak value of its realized gain pattern is maintained, its beamwidth is significantly enlarged.

The values of the differential reflection coefficient, i.e., $|S_{dd11}|$, of the antennas depicted in Figs. 2(a) and 2(b), are also provided in Fig. 3. In addition to the electric field distributions, the 3-D realized gain patterns of their resonant modes are displayed. The standard $TM_{03}$-mode behaviors are observed for both antennas, but the sidelobes of the $TM_{03}$ mode of the antenna in Fig. 2(b) are suppressed successfully. While the noted sidelobe suppression of the $TM_{03}$-mode occurs, it is also clear that the FR becomes less than 3 when the non-resonant slot is present.

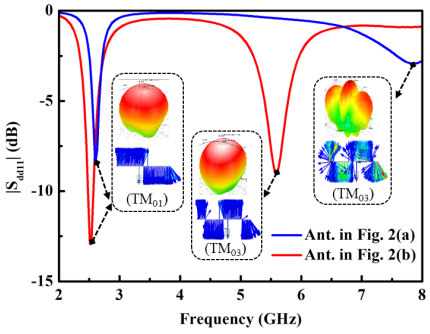


Fig. 3. Simulated differential reflection coefficients, i.e., $|S_{dd11}|$, of the MPAs shown in Figs. 2(a) and 2(b). The 3-D radiation patterns and electric field distributions of the corresponding resonant modes are given in the insets.

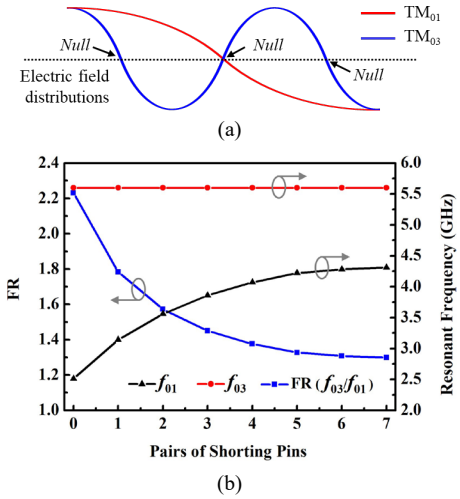


Fig. 4. The working principle of installing the shorting pins to adjust the FR of the dual-band differential-fed MPA. (a) Approximate electric field distributions of the $TM_{01}$ and $TM_{03}$ modes. (b) The resonance frequencies $f_{01}$ and $f_{03}$ and their frequency ratio ($f_{03}/f_{01}$) when the patch is loaded with different numbers of pairs of shorting pins.

It is noted from the sketch in Fig. 4(a) that the resonance frequency $f_{01}$ of the $TM_{01}$ mode can be independently adjusted by placing a pair of shorting pins around the null point of the electric field of the $TM_{03}$ mode. This arrangement has little impact on $f_{03}$. A similar phenomenon has been detailed in [24]. The results of our parametric studies of these two resonance frequencies and their frequency ratio ($f_{03}/f_{01}$) for the antenna depicted in Fig. 2(c) when different numbers of pairs of shorting pins are employed is presented in Fig. 4(b). It can be seen that $f_{03}$ remains fixed while $f_{01}$ is gradually shifted to a higher frequency when more shorting pins are present. We have determined that the corresponding achievable FR values range from 1.31 to 2.23. Since the second passband would remain unchanged, one could further adjust the FR value simply by loading the patch with yet more shorting pins. Nevertheless, additional simulations indicate that the filtering performance will degrade if one tries to pushe the lower or upper bounds of the FR value too far.

As a consequence, only two pairs of shorting pins were adopted in our DBDF design. They enable the differentially-fed MPA to cover commonly utilized frequency bands including, for example, the 3.5G and 5.2G bands. Herein, we have optimized the design to cover the 5G N78 band and part of the IEEE 802.11 ax 5 GHz band.

*Step 2) Improving the bandwidth and establishing the filtering performance*

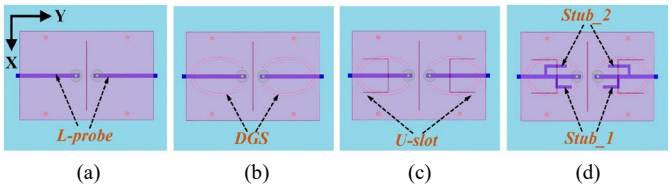


Fig. 5. Evolution through four differentially-fed MPA iterations to achieve the final DBDF design, each having large fractional bandwidths. (a) Ant. I. (b) Ant. II. (c) Ant. III. (d) Ant. IV, the final design.

The features added to the dual-band differential-fed MPA shown in Fig. 2(c) to attain the bandwidth and filter function enhancements were achieved through an evolutionary design sequence. The intermediary antennas of this evolution are illustrated in Fig. 5 for ease of comparison. Each antenna is realized by incorporating an additional structure into the previous one. These structures are:

(I) Differential L-shaped coupling feed probes (*L-probe*)
(II) A pair of open olive-shaped rings that are etched on the ground plane (*DGS*)
(III) A pair of U-slots etched on the patch (*U-slot*)
(IV) Two pairs of L-shaped open-end stubs loaded on the main strip of the L-probe (*Stub_1* and *Stub_2*)

The fourth iteration, Ant IV, was optimized as the final design.

Fig. 6 gives the simulated $|S_{dd11}|$ and realized gain values of these designs. In order to better distinguish them, the out-of-band radiation nulls are labeled as *RN1–RN5* in the sequence in which they appear. The in-band resonances of the upper passband are labeled as $f_1$–$f_3$ to concisely indicate their appearance.

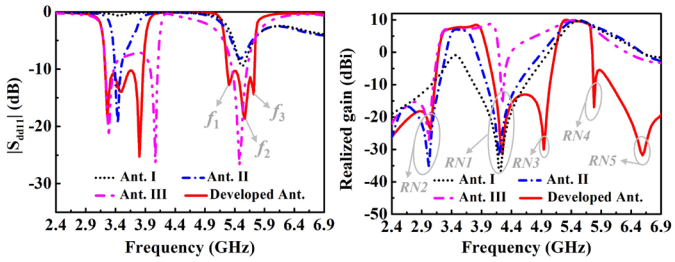


Fig. 6. Simulated results for the four differentially-fed MPA iterations as functions of the source frequency. (a) $|S_{dd11}|$ values. (b) Realized gain values.

The direct-probe fed antenna in Fig. 2(c) is modified first by simply replacing the simple coaxial probes with L-shaped feed probes as shown in Fig. 5(a). The dimensions of the design parameters remain unchanged. One can see in Fig. 6(b) that these L-probes induce a deep radiation null at the upper band-edge of the lower passband. This radiation null, *RN1*, improves the frequency selectivity and out-of-band suppression level of the lower operating band. It appears as a result of the interaction between the L-shaped probe and the patch. This phenomenon was clearly explained in our previous work [5].

The corresponding parametric study to determine the effect of the length $L_1$ of the probe on the *RN1* position is summarized with the results displayed in Fig. 7. Clearly, the L-probe-feed is indeed responsible for the radiation null and its length flexibly controls *RN1*. While good isolation between the two operating bands is realized with the L-probe being present, the bandwidth and frequency selectivity of these two bands are severely limited because there is only one resonance in the passband and only one radiation null in the stopband.

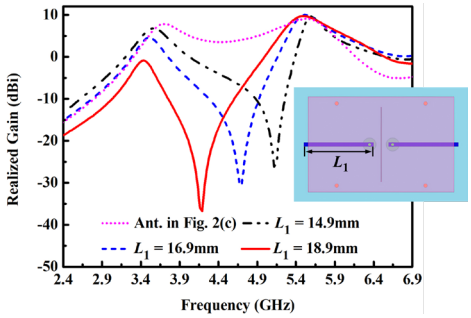


Fig. 7. Variation of the simulated realized gain values of the antenna in Fig. 2(c) and of Ant. I in Fig. 5(a) as the length, $L_1$, of L-shaped probe changes.

The next modification is realized by etching one pair of open olive-shaped rings on the ground plane of Ant. I with $L_1$ = 18.9 mm. This result is Ant. II in Fig. 5(b). Its DGS improves its frequency response. Fig. 6 indicates that one extra in-band resonance and one extra out-of-band radiation null, *RN2*, are produced. They, respectively, enhance the bandwidth and selectivity of the lower passband. The results of the parametric study of the olive shape by varying the length $R_2$ are given in Fig. 8. As $R_2$ increases from 4.8 to 5.2 mm, $RN_2$ red-shifts, the lower passband becomes wider, and the location of $RN_1$ remains unchanged. It can also be inferred that the newly introduced in-band resonance shown in Fig. 6(a) also exhibits a red-shift as $R_2$ increases. Therefore, it is concluded that not only does the DGS introduce a radiation null and an extra in-band resonance, it facilitates the independent control of the radiation null $RN_2$ by the shape of its open olive-shaped rings.

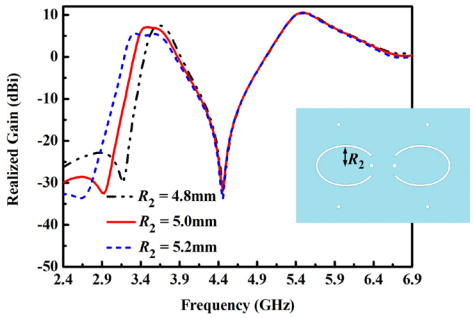


Fig. 8. Variation of the simulated realized gain values of Ant. II in Fig. 5(b) as the length $R_2$ changes.

As shown in Fig. 5(c), the third iteration, Ant. III, is obtained from Ant. II simply by etching a pair of half-wavelength U-shaped slots on the patch. Their introduction further enhances the bandwidth of the lower passband. One can also see in Fig. 6(a) that one extra resonance is introduced while there is little effect on the filter performance.

Finally, in order to improve the bandwidth and filtering features of the upper operating band, two pairs of L-shaped open-end stubs with different lengths (*Stub_1*, *Stub_2*) are attached to the main strip of the L-probe in Ant. III. This final design, Ant IV, is shown in Fig. 5(d). Fig. 6 clearly shows that not only are two in-band resonances generated that greatly enhance the operational bandwidth, but also that three new out-of-band radiation nulls, *RN3–RN5*, are simultaneously introduced. These nulls improve the frequency selectivity and suppression levels of the upper frequency band.

To further investigate how these additional nulls are generated, the current distributions on the feedlines at three frequency points, i.e., at the three out-of-band radiation nulls *RN3–RN5,* are shown in Fig. 9. Specifically, the current distributions at these three out-of-band radiation nulls: 4.94 (*RN3*), 5.78 (*RN4*), and 6.59 (*RN5*) GHz are shown in Figs. 9(a)–9(c), respectively. Fig. 9(a) shows the current at *RN3* being mainly concentrated on the *Stub_2*. The L-shaped open-end stub is short-circuited to the L-probe and acts as a quarter-wavelength resonator [25], i.e., its total length $L_5 + L_6 \approx \lambda_{g1}/4$, where $\lambda_{g1}$ is the guided wavelength in the substrate at the resonance frequency *RN3*. Consequently, *Stub_2* acts a resonant filter at *RN3*, i.e., the signal cannot flow along the feedlines at *RN3* and, thus, it cannot excite the radiating patch. Thus, the antenna is not excited and the null occurs. Likewise, as shown in Fig. 9(c), the majority of the current at *RN5* is concentrated on *Stub_1*. Its total length is $L_5 + L_6 \approx \lambda_{g2}/4$, where $\lambda_{g2}$ is the guided wavelength in the substrate at the resonance frequency *RN5*. Consequently, since it is also short-circuited to the L-probe, it acts as a quarter-wavelength resonant filter at *RN5*. Because the signal cannot flow in the feedlines at *RN5*, the patch is not excited and the null appears.

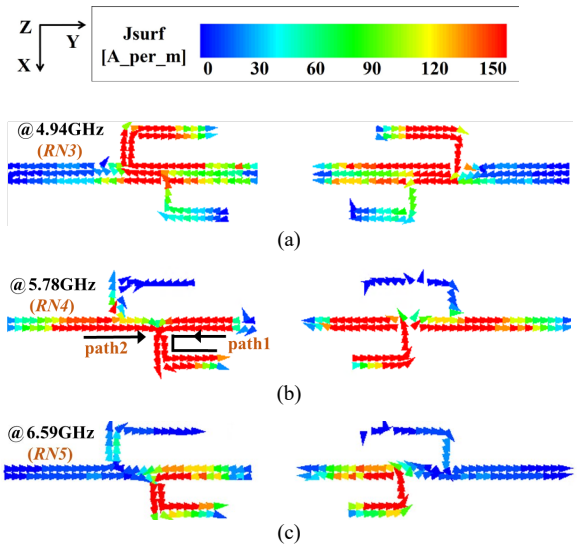


Fig. 9. The electric current distributions on the differential feedlines of the DBDF at the frequencies of nulls: (a) 4.94, (b) 5.78 and (c) 6.59 GHz.

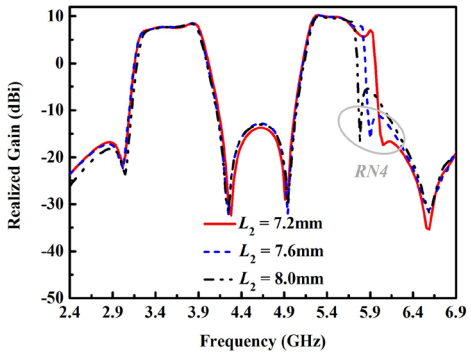


Fig. 10. Simulated realized gain values of the developed DBDF as the length $L_2$ of the main strip of the L-probes varies.

The current distribution at *RN4* is different from those of *RN3* and *RN5*. It is concentrated simultaneously on the L-probe and *Stub_1*. As illustrated in Fig. 9(b), two signal transmission paths, i.e., path1 and path2, occur. The two signal paths have equal amplitude, but opposite phase. Thus, L-probe and *Stub_1* are established as a cross-coupled

structure. This type of cross-coupled structure is known to generate a transmission zero of a filter [26]. Consequently, a radiation null occurs at *RN4* that is mainly dependent on the lengths of path1 and path2. Fig. 10 presents the relationship between *RN4* and the length $L_2$ of path2. It is clearly observed that *RN4* exhibits a red-shift, while the other radiation null frequencies remain almost unchanged.

Additionally, note that an effective electric wall is formed along the *x*-axis under the differential mode excitation. Thus, the differential feedlines can be treated as single-ended ones. Consequently, the L-probe and stubs system can be viewed as an asymmetrical dual-mode resonator with resonance frequencies $f_1$ and $f_3$. Due to the significant loading effect of the patch and the close proximity of $f_1$ and $f_3$ to $f_2$, the broadside radiation corresponding to $f_2$ dominates the entire passband, even at $f_1$ and $f_3$. The result is a quite flat broadside realized gain response over the entire upper band.

## III. Experimental Results

The optimized DBDF shown in Fig. 1 was fabricated, assembled, and tested, as shown in Fig. 11. The differential excitations for the measurements were provided by a hybrid coupler shown in Fig. 11(b). Eight polyamide pillars were utilized to bond the two substrates together to ensure the mechanical stability of the filtenna during the measurement process, as indicated in Fig. 11(c). The far-field characteristics were obtained in a chamber as shown in Fig. 11(c).

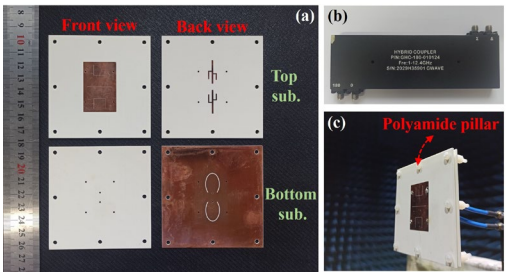


Fig. 11. Fabricated DBDF. (a) Front and back views of each layer before assembly. (b) The hybrid coupler. (c) Antenna under test in the chamber.

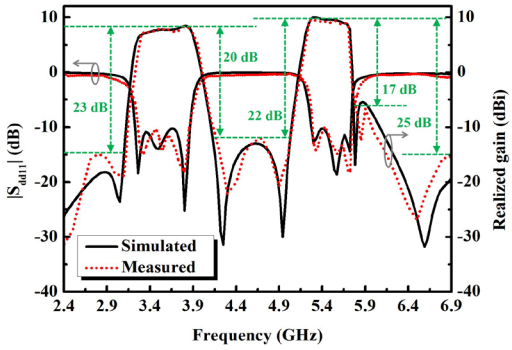


Fig. 12. Measured and simulated $|S_{dd11}|$ and realized gain values of the optimized DBDF.

The measured and simulated performance characteristics of the optimized DBDF are displayed in Fig. 12. The measured –10-dB impedance fractional bandwidths (IFBWs) are 17.5% (3.23–3.85 GHz) and 8.2% (5.29–5.74 GHz) for the lower and upper operating bands, respectively. In comparison, the simulated values are 18.4% (3.23-3.87 GHz) and 8.4% (5.27-5.73 GHz). With reference to the corresponding realized gain curves, the measured peak values for the two bands are 8.4 and 9.5 dBi, while the simulated ones are about 8.4 and 10.1 dBi. There are reasonable, small disparities between the measured and simulated results. These differences are mainly due to fabrication errors and measurement inaccuracies. As designed, there are five deep radiation nulls. They provide a quasi-elliptic band-pass response in both bands with high frequency selectivity and strong suppression levels. The measured stopband suppression levels at the lower and upper band-edges of the lower (higher) frequency band are 23 (22) dB and 20 (17) dB, respectively. These levels and values are highlighted in green. Note that there is a visible increase in the gain around 5.9 GHz. This feature allows for an acceptable decrease in the suppression level of the upper stopband of the higher frequency band. To overcome this droop, a deep null in the gain at 6.5 GHz was created, which leads to a significant improvement in the upper stopband suppression level from 17 to 25 dB.

Fig. 13 shows the measured and simulated radiation patterns of the prototype at 3.5 (lower passband) and 5.5 (upper passband) GHz. Again, good agreement is observed between them. It is clearly that the peak realized gain is strictly in the broadside direction. Moreover, the measured co-polarized fields in both principal planes in that direction for both operating bands are at least 44 dB and 40 dB stronger than their cross-polarized counterparts, respectively.

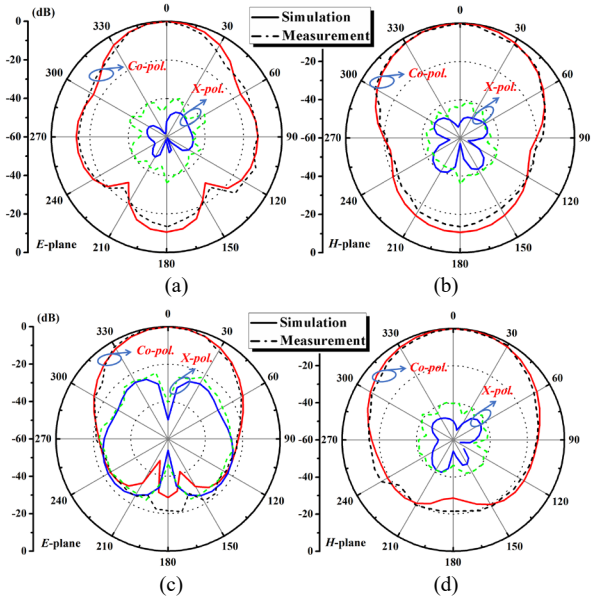


Fig. 13. Radiation patterns at 3.5 GHz in the (a) *E*-plane and (b) *H*-plane; and at 5.5 GHz in the (c) *E*-plane and (d) *H*-plane.

Detailed comparisons of the performance characteristics of our DBDF prototype with the other recently reported dual-band filtenna systems are given in Table II. The operational bandwidths of the two bands in [18] were only 1.3% and 0.7% as a consequence of only one resonant mode being present in each band. Similarly, the operational bandwidths of the two frequency bands in [19] were only 2.4% and 5.2% as a consequence of there being only two resonant modes present in each band. Although comparable bandwidths were obtained in both of the operating frequency bands in [20], the system occupies a much larger transverse size (~3.6 times) and has a relatively higher profile (~2 times) than our design. These differences are attributed to the complex feed network in that system. The frequency selectivity at the lower and upper band-edges of each operating band, denoted as $F_L$ and $F_U$, is quantified as [4]:

$$F_L = \frac{f_{10L} - f_{\Delta 20L}}{f_{10U} - f_{10L}} \qquad F_U = \frac{f_{\Delta 20U} - f_{10U}}{f_{10U} - f_{10L}} \tag{2}$$

The terms $f_{10L}$ and $f_{10U}$ are, respectively, the frequencies at which $|S_{dd11}| = -10$ dB at the lower and upper band-edges of the passband. Similarly, the terms $f_{\Delta 20L}$ and $f_{\Delta 20U}$ are, respectively, the lower and upper frequencies corresponding to the 20 dB gain suppression values with respect to the gain at the center frequency $f_0$. Better frequency selectivity is represented by smaller $F_L$ or $F_U$ values in this work.

According to the $F_L$ and $F_U$ values in Table II, it is recognized that our design has higher frequency selectivity in both bands in comparison to those in [18]-[20]. This feature arises from our design having more radiation nulls. Finally, our design is appreciably more compact in size, has a very acceptable low profile, has smaller cross-pol levels, and has comparable peak realized gain values.

TABLE II
COMPARISONS OF THE DBDF PROTOTYPE WITH THE DIFFERENTIAL DUAL-BAND FILTENNAS REPORTED RECENTLY IN THE LITERATURE

| Refs. | Profile ($*\lambda_0$) | Size ($*\lambda_0^2$) | IFBW | Peak Real. Gain (dBi) | $F_L/F_U$ for Lower (upper) band, Num. of Nulls | Cross -Pol. Level (dB) |
|---|---|---|---|---|---|---|
| [18] | 0.01 | 0.67*0.62 = 0.415 | 1.3% / 0.7% | 7.2 / 6.8 | 6/7 (9.16/5.83), 2 | 37/32 |
| [19] | 0.02 | 0.4*0.49 = 0.196 | 2.4% / 5.2% | 5.45 / 8.5 | 2.8/2.8 (1.83/2.17), 0 | 27/32 |
| [20] | 0.13 | 0.75*0.75 = 0.563 | 16.7% / 9% | 8.7 / 9.8 | 1.15/1.38 (0.79/1.65), 3 | 30/30 |
| This work | **0.065** | **0.31*0.5 = 0.155** | **17.5% / 8.2%** | **8.4 / 9.5** | **0.68/0.87 (0.95/0.59), 5** | **44/40** |

## IV. CONCLUSION

A DBDF with wide bandwidths and high-selectivity in both of its filtering passbands, as well as high broadside peak realized gain values and low cross-polarization levels in its antenna function over those bands, was developed in this paper. The design employed a dual-mode patch radiating in its $TM_{01}$ mode to create its lower passband and in a reshaped $TM_{03}$ mode to create its upper passband. Two pairs of shorting pins were introduced to facilitate tuning the FR between these two bands. A pair of specially-engineered stub-loaded differential feedlines expanded the operating bandwidths and enhanced the selectivity and out-of-band suppression levels of both bands by introducing additional in-band resonances and radiation nulls.

A prototype of the optimized DBDF was fabricated and tested. It is compact in size ($0.31\ \lambda_0 \times 0.5\ \lambda_0$) and has a low profile ($\lambda_0$ / 15.38). The measured results confirm that it attained maximum realized gains of 8.4 and 9.5 dBi in its broadside direction, and –10-dB IFBWs of 17.5% and 8.2% for the lower and upper passbands, respectively. The developed DBDF possesses significant potential for application in many space-limited platforms related to satellite communications, electronic countermeasures, and radar detection systems.

## REFERENCES


[1] W. Wang, X. Liu, Y. Wu, and Y. Liu, "A broadband filtering patch antenna using T-probe, transverse stubs, and U-Slots," *IEEE Access*, vol. 7, pp. 7502–7509, 2019.

[2] Y.-M. Pan, P.-F. Hu, X.-Y. Zhang, and S.-Y. Zheng, "A low-profile high-gain and wideband filtering antenna with metasurface," *IEEE Trans. Antennas Propag.*, vol.64, no.5, pp. 2010–2016, May 2016.

[3] P.-F. Hu, Y.-M. Pan, X.-Y Zhang, and B.-J. Hu, "A filtering patch antenna with reconfigurable frequency and bandwidth using F-shaped probe," *IEEE Trans. Antennas Propag.*, vol. 67, no. 1, pp. 121–130, Jan. 2019.

[4] K. Xu, J. Shi, X. Qing , Z. N. Chen, "A substrate integrated cavity backed filtering slot antenna stacked with a patch for frequency selectivity enhancement," *IEEE Antennas Wireless Propag. Lett.,* vol. 17, no. 10, pp. 1910–1914, Oct. 2018.

[5] M.-C. Tang, D. Li, Y. Wang, K.-Z. Hu, and R. W. Ziolkowski, "Compact, low-profile, linearly and circularly polarized filtennas enabled with custom-designed feed-probe structures," *IEEE Trans. Antennas Propag.*, vol. 68, no. 7, pp. 5247–5256, Jul. 2020.

[6] K. Dhwaj, H. Tian, and T. Itoh, "Low-profile dual-band filtering antenna using common planar cavity," *IEEE Antennas Wireless Propag. Lett.*, vol. 17, pp. 1081–1084, 2018.

[7] C. X. Mao, S. Gao, Y. Wang, Benito Sanz-Izquierdo, Z. Wang, F. Qin, Q.-X. Chu, J. Li, G. Wei, and J. Xu, "Dual-band patch antenna with filtering performance and harmonic suppression," *IEEE Trans. Antennas Propag.*, vol. 64, no. 9, pp. 4074–4077, Sep. 2016.

[8] X. Y. Zhang, Y. Zhang, Y. M. Pan, and W. Duan, "Low-profile dual-band filtering patch antenna and its application to LTE MIMO system," *IEEE Trans. Antennas Propag.*, vol. 65, no. 1, pp. 103–113, Jan. 2017.

[9] C.-Y. Hsieh, C.-H. Wu, and T.-G. Ma, "A compact dual-band filtering patch antenna using step impedance resonators," *IEEE Antennas Wireless Propag. Lett.*, vol. 14, pp. 1056–1059, 2015.

[10] P. F. Hu, Y. M. Pan, K. W. Leung, and X. Y. Zhang, "Wide-/dual-band omnidirectional filtering dielectric resonator antennas," *IEEE Trans. Antennas Propag.*, vol. 66, no. 5, pp. 2622–2627, May 2018.

[11] J.-F. Qian, F.-C. Chen, and Q.-X. Chu, "A novel tri-band patch antenna with broadside radiation and its application to filtering antenna," *IEEE Trans. Antennas Propag.*, vol. 66, no. 10, pp. 5580–5585, Oct. 2018.

[12] W. Yang, M. Xun, W. Che, W. Feng, Y. Zhang, and Q. Xue, "Novel compact high-gain differential-fed dual-polarized filtering patch antenna," *IEEE Trans. Antennas Propag.*, vol. 67, no. 12, pp. 7261–7271, Dec. 2019.

[13] H.-T. Hu, F.-C. Chen, J.-F. Qian, and Q.-X. Chu, "A differential filtering microstrip antenna array with intrinsic common-mode rejection," *IEEE Trans. Antennas Propag.*, vol. 65, no. 12, pp. 7361–7365, Dec. 2017.

[14] H. Tang, C. Tong, and J.-X. Chen, "Differential dual-polarized filtering dielectric resonator antenna," *IEEE Trans. Antennas Propag.*, vol. 66, no. 8, pp. 4298–4302, Aug. 2018.

[15] C. W. Tong, H. Tang, J. Li, W. W. Yang, and J. X. Chen, "Differentially coplanar-fed filtering dielectric resonator antenna for millimeter-wave applications," *IEEE Antennas Wireless Propag. Lett.*, vol. 18, no. 4, pp. 786–790, Apr. 2019.

[16] X.-Y. Wang, S.-C. Tang, L.-L. Yang, and J.-X. Chen, "Differential-fed dual-polarized dielectric patch antenna with gain enhancement based on higher order modes," *IEEE Antennas Wireless Propag. Lett.*, vol. 19, no. 3, pp. 502–506, Mar. 2020.

[17] J. Shi, X. Wu, Z. N. Chen, X. Qing, L. Lin, J. Chen, and Z.-H. Bao, "A compact differential filtering quasi-Yagi antenna with high frequency selectivity and low cross-polarization levels," *IEEE Antennas Wireless Propag. Lett.*, vol. 14, pp. 1573–1576, 2015.

[18] Y. Li, Z. Zhao, Z. Tang, and Y. Yin, "Differentially fed, dual-band filtering antenna with H-shaped slot," *Microwave and Optical Technology Letters*, vol. 62, no. 1, pp. 448–452, Jan. 2020.

[19] D. Li, M.-C. Tang, Y. Wang, K.-Z. Hu, and R. W. Ziolkowski, "Compact differential diplex filtenna with common-mode suppression for highly integrated radio frequency front-ends," *IEEE Trans. Antennas Propag.*, vol. 69, no. 11, pp. 7935-7940, Nov. 2021.

[20] Y. Li, Z. Zhao, Z. Tang, and Y. Yin, "Differentially-fed, dual-band dual-polarized filtering antenna with high selectivity for 5G sub-6 GHz base station applications," *IEEE Trans. Antennas Propag.*, vol. 68, no. 4, pp. 3231–3236, Apr. 2020.

[21] Y. P. Zhang and J. J. Wang, "Theory and analysis of differentially-driven microstrip antennas," *IEEE Trans. Antennas Propag.*, vol. 54, no. 4, pp. 1092–1099, Apr. 2006.

[22] Y. T. Lo, D. Solomon, and W. Richards, "Theory and experiment on microstrip antennas," *IEEE Trans. Antennas Propag.*, vol. 27, no. 2, pp. 137–145, Mar. 1979.

[23] X. Zhang, L. Zhu, and Q.-S. Wu, "Sidelobe-reduced and gain-enhanced square patch antennas with adjustable beamwidth under $TM_{03}$ mode operation," *IEEE Trans. Antennas Propag.*, vol. 66, no. 4, pp. 1704–1713, Apr. 2018.

[24] S. S. Zhong and Y. T. Lo, "Single-element rectangular microstrip antenna for dual-frequency operation," *Electron. Lett.*, vol. 19, no. 8, pp. 298–300, Apr. 1983.

[25] D. M. Pozar, *Microwave Engineering*. New York: Wiley, 2005.

[26] R. J. Cameron, C. M. Kudsia, and R. R. Mansour, *Microwave Filters for Communication Systems: Fundamentals, Design and Applications*. New York, NY, USA: Wiley, 2007.